



1 **Mobile evaporite enhances the cycle of physical–chemical**
2 **erosion in badlands**

3 Ci-Jian Yang^{1, 2}, Pei-Hao Chen¹, Erica D. Erlanger², Jens M. Turowski², Sen Xu², Tse-Yang Teng³,

4 Jiun-Chuan Lin¹, Jr-Chuang Huang¹

5 1.Department of Geography, National Taiwan University, No. 1, Sec. 4, Roosevelt Rd., Taipei 10617, Taiwan.

6 2.German Research Centre for Geosciences (GFZ), Telegrafenberg 14473, Potsdam, Germany.

7 3.Sustain-vision Consulting Co. Ltd., Taipei 11168, Taiwan.

8 *Correspondence to:* Ci-Jian Yang (d03228001@ntu.edu.tw)

9 **Abstract.** Chemical weathering driven by physical erosion is one of the manifestations of natural
10 processes that strongly affect chemical and solid matter budgets at the Earth's surface. However, the
11 influence of extreme climatic erosion on chemical weathering dynamics is poorly understood. Badland
12 landscapes formed in highly erodible, homogeneous substrates have the potential to respond to
13 individual events on scales that are rapid enough for direct observation. Here, we assess the
14 geochemical and grain-size composition of suspended sediment and riverine chemistry measurements
15 collected from two catchments during the 2017 Nesat and Haitang typhoons in southwestern Taiwan.
16 During the typhoons, the sodium adsorption ratio covaried with suspended sediment concentration,
17 which we attributed to sodium-induced deflocculation. Evaporite weathering at peak rainfall is
18 succeeded by peak silicate weather at maximum discharge, which dominates the weathering signal of
19 the event. Overall, our observations suggest that initial weathering of near-surface evaporite enhances
20 the physical erosion of silicate rock during extreme rainfall events.
21



22 **1. Introduction**

23 Chemical weathering induced by physical erosion controls nutrient supply to ecosystems (Milligan
24 and Morel, 2002), reflects dynamic surface processes (e.g., Calmels et. al., 2011; Clift et. al., 2014;
25 Emberson et. al., 2016; Meyer et. al., 2017), and regulates the global carbon cycle and the evolution
26 of Earth's long-term climate (Bernier et al., 1983; Ram et al., 1992; Gaillardet et al., 1999). In most
27 landscapes, physical erosion and chemical weathering operate on geological timescales (e.g., Maher
28 et al., 2014). However, studies show that most erosion occurs during stochastic events, such as storms
29 (e.g., Lee et al., 2020; Wang et al., 2021). In particular, typhoons are able to transport large volumes
30 of water and dissolved solids within hours to days, allowing us to observe the interactions between
31 physical erosion and chemical weathering. Nevertheless, observations of the interaction between
32 extreme physical erosion and chemical weathering dynamics are limited (Meyer et. al., 2017). Lack of
33 high-frequency stream water sampling leads to a fundamental difficulty in constraining the dynamic
34 behavior between physical erosion and chemical weathering during a high discharge period (e.g., a
35 typhoon), which could have key implications for the quantification of topographic responses.

36

37 Badlands are landscapes characterized by highly erodible and weathered substrates, which are largely
38 devoid of vegetation. The high erodibility of these landscapes provides a unique opportunity to
39 investigate and quantify denudation processes that operate at short timescales (Cheng et al., 2019;
40 Yang et al, 2019, 2021a; 2021b). Soils that contain clays saturated in sodium ions are particularly
41 vulnerable to erosion by water. Sodium ions alter the layer charge of double-layered clay minerals (i.e.
42 smectite) and cause the clays to deflocculate, which refers to the process of breaking up the clay (and
43 ultimately the soil) into finer particles that are more easily washed away by water (e.g., Faulkner et al.,
44 2004; Mitchell et al., 1993; Rengasamy and Olsson, 1991; Rengasamy et al., 1984; Sherard et al., 1976;
45 Kašanin-Grubin et. al., 2018). Additionally, mineral assemblage affects the stability of soil aggregates;
46 for example, small amounts of smectite in kaolinitic materials cause it to be more dispersive and
47 unstable (Levy et al., 1993).



48

49 Previous studies in the badlands of SW Taiwan have revealed that dissolving halite and gypsum at
50 depth migrate to the slope surface and deposit in desiccation cracks during the dry season (Higuchi et
51 al., 2013, 2015; Nakata and Chigira, 2009). This produces pore water in the near-surface mudstone
52 with a concentration of Na^+ of 1–3 million $\mu\text{mol/L}$ at 1–2 cm depth (Nakata and Chigira, 2009). We
53 hypothesize that the dissolving halite and gypsum re-crystallizes near-surface and is deposited in the
54 mudstone cracks through capillary action during the dry season. Subsequent extreme precipitation
55 dissolves the evaporite, which enhances erosion by clay dispersity and further exposes more
56 weatherable materials, forming a positive feedback cycle. Assuming a mudstone substrate that is
57 primarily comprised of silicate minerals, we expect that the concentration of the evaporite ions should
58 be consistent with the changes in the sediment concentration and the concentration of silicate ions.

59

60 To investigate the relationship between evaporite dissolution and erosion, we use suspended sediment
61 concentrations (SSC) and stream chemistry data from two catchments in the badlands of SW Taiwan
62 (Fig. 1), collected with a temporal resolution of 3 hours. We interpret our observations in badlands to
63 reflect how the excess sodium enhances physical erosion and chemical weathering during a typhoon
64 event, and the importance of this process for exposing fresh bedrock available for weathering in the
65 following dry season.

66

67 **2. Geological and Meteorological Setting**

68 In Taiwan's badlands, the annual precipitation exceeds 2 m, and 90% of the rainfall is concentrated in
69 the rainy season. The rainy season lasts from May to October and reaches its peak in August, with over
70 400 mm of precipitation within a single month. In contrast, less than 40 mm of average monthly rainfall
71 is measured from November to April. We collected river water samples from two sites downstream of
72 the studied badland areas. The first site, Nanxiong Bridge (NX), is located at the midstream of the
73 Erren River and has a drainage area of 175 km^2 . This area includes badlands covering an area of 4.37

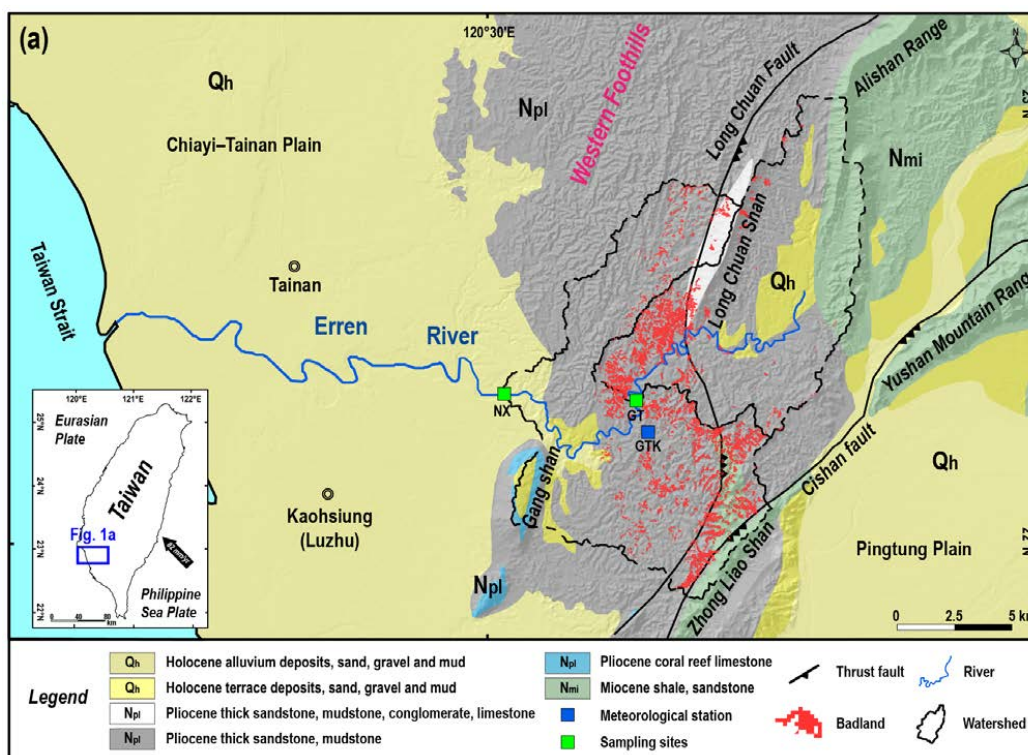


74 km², which accounts for 2.49% of the total catchment area (Fig.1). The Erren River catchment is
75 predominantly underlain by Plio-Pleistocene mudstones, which are several kilometers thick, and
76 mainly feature illite (30.54%) and chlorite (28.70%) minerals (Tsai, 1984a). During the dry seasons,
77 the pore water chemistry in the near-surface mudstones is mainly composed of Na⁺, Cl⁻, Ca²⁺ and SO₄²⁻
78 (Nakata and Chigira, 2009).

79

80 The gauging station at Nanxiong Bridge (NX) provides hourly discharge data for calculating sediment
81 and solute fluxes. The annual average discharge of Nanxiong Bridge station is 10.2 m³/s, and the
82 typhoon season accounts for 84% of the total discharge. The meteorological station at Gutingkeng
83 (GTK) is located 5.5 km from Nanxiong Bridge and provides hourly precipitation data. Our second
84 sampling site is Guting (GT) Bridge, with an upstream drainage area of 79 km² and a badlands area of
85 1.87 km², corresponding to 2.37% of the total area. Guting Bridge is located adjacent to a badlands
86 conservation area, so the riverine water chemistry reflects the weathering products derived from the
87 adjacent hillslopes. Due to a lack of stream discharge observations at Guting Bridge, we use hourly
88 precipitation data at GTK, which is less than 1 km from the sampling site, to quantify the impact of
89 the typhoon events.

90



91

92 **Figure 1.** Location of sampling sites and geology of the study area. (a) The geological map of the
93 study area (Source: Central Geological Survey, 2013). The green squares are sampling sites; hourly
94 stream discharge data were obtained from the Nanxiong Bridge (NX) hydrometric station (Water
95 Resources Agency). The blue square is the meteorological station, which provides hourly precipitation
96 data (Central Weather Bureau, <https://dbar.pccu.edu.tw/>).

97

98 3. Methods and Materials

99

3.1 Water Sampling

100

We collected 42 stream samples from the two sampling sites for the typhoon period of July 2017.

101

During sample collection, two 1000 ml PE bottles were dropped 1 to 2 meters below the water surface

102

of the river simultaneously. Suspended sediment concentration (SSC) was subsequently calculated

103

from the water collected in one of the PE bottles, and riverine chemistry was determined from water

104

collected in the other bottle. Samples were filtered *in situ*, and the filtrate was preserved in the

105

refrigerator for laboratory analysis. Additionally, 31 samples were collected from September 2014 to



106 December 2016 in the second half of every month at Nanxiong Bridge for non-typhoon periods, using
107 the same sampling procedure.

108

109 **3.2 Dissolved load and sediment chemistry analysis**

110 For the riverine dissolved load, we measured major dissolved anions (Cl^- , SO_4^{2-} , NO_2^- , NO_3^- , F^-) on an
111 Ion chromatography (IC, Metrohm Basic-883 plus), and we measured major dissolved cations (Na^+ ,
112 K^+ , Mg^{2+} , Sr^{2+} , Ba^{2+} , Si^{4+}) on an ICP-OES (PerkinElmer, Optima 2100DV). We measured bulk
113 sediment chemistry from two samples of suspended sediment collected from Guting Bridge at low
114 flow before the typhoon event ($2.26 \text{ m}^3/\text{s}$) and at the peak of runoff ($724.32 \text{ m}^3/\text{s}$). About 0.7 g of dried
115 sediment sample was combusted in the muffle furnace at 650°C for 2 hours and then weighed to obtain
116 the loss on ignition (LOI). Afterwards, an aliquot of $\sim 100 \text{ mg}$ from the residue was digested with a
117 mixture of concentrated HF and aqua regia. After digestion and drying, the sample was dissolved in
118 0.3 N HNO_3 for elemental determination. Major elemental concentrations of sediment samples were
119 obtained by ICP-OES (Varian 720-ES) at the GFZ German Research Centre for Geosciences.

120

121 **3.3 Grain size of suspended load**

122 Before measuring grain size, we removed the non-clastic deposition, i.e., sea salt, organic matter, and
123 carbonate. To remove sea salt, $\sim 1 \text{ g}$ of dried sediment sample was added to 15 ml of distilled water,
124 placed in a shaker, and shaken at a speed of 4000 rpm for 5 minutes. The centrifuged supernatant was
125 then poured out and these steps were repeated 3 times. To remove organic matter, 10 ml of a 15%
126 H_2O_2 solution was added to the sediment and placed in an ultrasonic oscillator for 24 hours. After
127 adding a second 10 ml of H_2O_2 (15%) to confirm the completion of the reaction, the mixture was
128 centrifuged and the supernatant containing the organic matter was removed. The sediment was then
129 washed by adding 30 ml of distilled water, and the supernatant was again removed after centrifugation.
130 This washing step was repeated 3 times to remove residual H_2O_2 in the centrifuge tube. To remove the



131 carbonates, we added 10 ml of 10% HCl solution to the centrifuge tube and allowed the acid to react
132 with the sediments for 24 hours. An additional 10 ml of HCl was then added to confirm the
133 completeness of the reaction. The sample was then centrifuged, and the supernatant was decanted to
134 remove the carbonates. The sample was then rinsed with 30 ml of distilled water, centrifuged, and
135 decanted. This step was performed 3 times to remove any residual HCl.

136

137 To disperse sediment agglomeration, we added 10 ml of 1% $\text{Na}(\text{PO}_3)_6$ solution to the sediment and let
138 the sample react for more than half a day. The grain size of the sediment samples was obtained by
139 Laser Diffraction Particle Size Analyzer LA950 at the GFZ German Research Centre for Geosciences.
140 By using LA950, we measured grains in the size range of between 100 nm to about 3 cm.

141

142 **3.4 Calculation of the enriched ratio and sodium adsorption ratio (SAR)**

143 In order to classify the supply of different ion sources during the typhoon event, we used the enriched
144 ratio of concentration as a reference. The enriched ratio is the ion concentration at a certain time
145 divided by the ion concentration at the first observation. A value greater than 1 represents a point in
146 time when the sample is more concentrated relative to the first observation, whereas a value smaller
147 than 1 represents a point in time when the sample is more diluted relative to the first observation.

148

149 Dissolved calcium and magnesium can stabilize soil aggregates and therefore facilitate water
150 permeability (Nadler et al., 1996). By contrast, excess sodium can disperse soil particles through
151 deflocculation, thereby reducing water permeability (Hanson et al., 1999). The potential for material
152 dispersion in badlands is generally determined by measuring the presence and behavior of sodium and
153 is quantified by the sodium absorption ratio (SAR), (1):

$$154 \quad SAR = \frac{Na^+}{\sqrt{\frac{Ca^{2+} + Mg^{2+}}{2}}} \quad (1)$$



155 When SAR is greater than 13, the excess sodium causes soil particles to repel each other, preventing
156 the formation of soil aggregates (Seelig, 2000; Horneck et al., 2007).

157

158 **3.5 Calculation of TDS and chemical weathering rate**

159 Riverine TDS is widely used to estimate chemical weathering rates of river catchments (e.g. Gaillardet
160 et al. 1999). In this study, riverine TDS (in units of $\mu\text{mol/L}$) is expressed as:

$$161 \quad TDS = TDS_{rain} + TDS_{evaporite} + TDS_{sil} + TDS_{carb} \quad (2)$$

162 where the contributions from precipitation (TDS_{rain}), evaporite ($TDS_{evaporite}$), silicate weathering
163 (TDS_{sil}) and carbonate weathering (TDS_{carb}) are considered. We calculated the proportions of ion
164 contributions with the MEANDIR inversion model (Kemeny and Torres, 2021), a MATLAB script for
165 inverting fractional contributions of end-members, and for constraining the chemical compositions of
166 those end-members. To exclude the input of precipitation (TDS_{rain}) from riverine TDS, we used local
167 rainwater Cl^- concentrations with an average value of $68 \mu\text{mol/L}$ (Lu, 2014), and also the ratios of Cl^-
168 and SO_4^{2-} , Na^+ , K^+ , Mg^{2+} , Ca^{2+} in rainfall based on the rainfall chemistry from 2007 to 2013 ($\text{SO}_4^{2-}/$
169 $\text{Cl}^- = 0.35$, $\text{Na}^+/\text{Cl}^- = 0.90$, $\text{K}^+/\text{Cl}^- = 0.09$, $\text{Mg}^{2+}/\text{Cl}^- = 0.18$, $\text{Ca}^{2+}/\text{Cl}^- = 0.35$) (Lu, 2014). Thus, we
170 estimated the annual deposition of those cations using equation (3):

$$171 \quad [X]_{norain} = [X]_{river} - [X]_{rain} \quad (3)$$

$$172 \quad TDS_{rain} = \sum [X]_{rain} \quad (4)$$

173 Here $[X]_{norain}$ reflects the remaining concentration of ion X after the removal of atmospheric
174 inputs; $[X]_{river}$ is the concentration of ion X in river water, and $[X]_{rain}$ is the concentration of ion X from
175 atmospheric deposition. In the second step, we corrected for evaporite inputs ($TDS_{evaporite}$) using the
176 following equation:

$$177 \quad [X]_{NSS} = [X]_{norain} - [X]_{evap} = [X]_{norain} - \left([Cl]_{norain} \times \left(\frac{X}{Cl} \right)_{evap} \right) \quad (5)$$

$$178 \quad TDS_{evaporite} = \sum [X]_{evap} \quad (6)$$



179 where $[X]_{\text{NSS}}$ is the concentration of ion X after the removal of ions attributed to evaporites, $[X]_{\text{evap}}$.
180 $[X/\text{Cl}]_{\text{evap}}$ is the ratio of ion X and Cl by using the end-member molar ratios of evaporite ($\text{SO}_4^{2-}/\text{Cl}^- =$
181 0.4, $\text{Na}^+/\text{Cl}^- = 1$, $\text{Mg}^{2+}/\text{Cl}^- = 0.10$, $\text{Ca}^{2+}/\text{Cl}^- = 0.5$, Burke et al., 2018; $\text{K}^+/\text{Cl}^- = 0.026$, Chao et al., 2013).
182 Then, after the correction for evaporite, the chemical weathering budget can be divided into
183 contributions by silicate (TDS_{sil}) and carbonate weathering (TDS_{carb}), expressed as:

$$184 \quad \text{TDS}_{\text{sil}} = [\text{Na}]_{\text{sil}} + [\text{K}]_{\text{sil}} + [\text{Mg}]_{\text{sil}} + [\text{Ca}]_{\text{sil}} + [\text{SiO}_2]_{\text{sil}} \quad (7)$$

$$185 \quad \text{TDS}_{\text{carb}} = [\text{Mg}]_{\text{carb}} + [\text{Ca}]_{\text{carb}} + [\text{HCO}_3]_{\text{carb}} \quad (8)$$

$$186 \quad [\text{HCO}_3]_{\text{carb}} = \frac{1}{2}([\text{Mg}]_{\text{carb}} + [\text{Ca}]_{\text{carb}}) \quad (9)$$

187 where $[\text{Na}]_{\text{sil}}$ and $[\text{K}]_{\text{sil}}$ are riverine $[\text{Na}]_{\text{NSS}}$ and $[\text{K}]_{\text{NSS}}$ concentration, respectively. We used
188 endmember values for silicate- and carbonate-dominated rocks reported by Gaillardet et al. (1999),
189 which gave ratios of $\text{Ca}/\text{Na} = 0.35$ and $\text{Mg}/\text{Na} = 0.24$ for silicates, and $\text{Ca}/\text{Na} = 50$ and $\text{Mg}/\text{Na} = 10$ for
190 carbonates.

191

192 4. Results

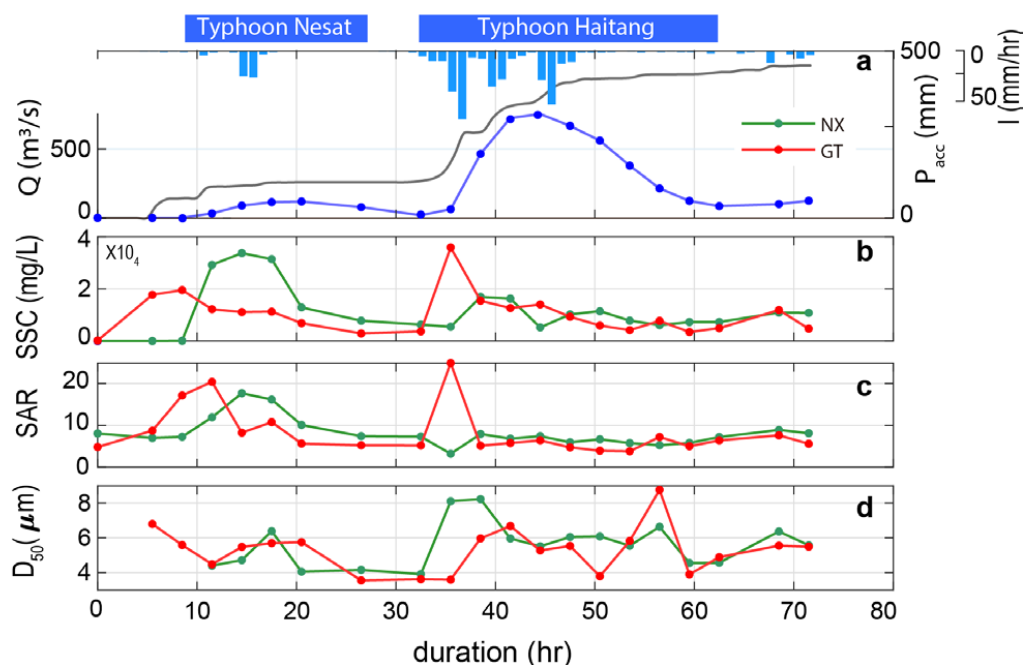
193 4.1 Geochemistry of river water and suspended sediment

194 In 2017, the Nesat and Haitang typhoons brought 579 mm of rainfall over three days, with a maximum
195 intensity of 74 mm/hr. The discharge at Nanxiong Bridge demonstrated that the climatic co-response
196 has two pulses (Fig. 2). Since the time interval between the two typhoons was less than 6 hours, we
197 define the two typhoons as one typhoon event and distinguish between a first and second discharge
198 pulse. We quantify time relative to the onset of the typhoon (0 hr). The first pulse occurred from 8.5 to
199 32.5 hr, with a mean water discharge of $66.2 \text{ m}^3/\text{s}$. The second pulse that occurred from 32.5 to 62.5
200 hr had a 5.5 times higher mean discharge of $369.2 \text{ m}^3/\text{s}$. The maximum discharge ($753.2 \text{ m}^3/\text{s}$) was
201 observed during the second pulse at 44.5 hr (July 31th, 2017, at 6:00 a.m.) (Fig. 2).

202



203 At Nanxiong Bridge, SSC has a statistically significant positive correlation with SAR ($\rho = 0.51$, $p <$
 204 0.05). SSC has two peaks during the both pulses, but SAR only shows a peak during the first pulse.
 205 During the first pulse, SSC ranged from 10 to 33757 mg/L and SAR increased from 8.2 and to 17.7.
 206 During the second pulse, SSC increased from 5445 to 16900 mg/L and SAR is steadily about 7.3.
 207 D_{50} ranged from 3.9 to 8.2 μm , with an average value of 5.6 μm during the second pulse, and exhibited
 208 a positive correlation with discharge ($\rho = 0.40$). At Guting Bridge, SSC has a statistically significant
 209 positive correlation with SAR ($\rho = 0.69$, $p < 0.05$) during the survey. SSC ranged from 164 to 19538
 210 mg/L before the first pulse and ranged from 2857 to 35920 mg/L during the second pulse, while SAR
 211 showed a mean of 8.2 and two peaks with a value over 20 during both pulses. D_{50} ranged from 3.6 to
 212 8.8 μm , with an average value of 5.3 μm during the second pulse, (Fig. 2). In terms of sediment
 213 chemistry at Guting Bridge, major elements of the two selected sediment samples show that calcium
 214 and sodium accounted for about 10% of the mass loss between the typhoon event (5.5 hr of duration)
 215 and peak of discharge (41.5 hr of duration) (Table. S4).



216
 217 **Figure 2.** Timeseries SSC, SAR and median grain size of suspended sediment (D_{50}) at two sampling
 218 sites. The blue line denotes hourly discharge (Q) at Nanxiong Bridge, and the blue bar denotes hourly



219 precipitation (I) at Gutingkeng station. The gray line denotes precipitation accumulation (P_{acc}), the
220 green line denotes the Nanxiong Bridge (NX) dataset, and the red line denotes the Guting Bridge (GT)
221 dataset.

222

223 The fractional proportions of TDS at Nanxiong Bridge during baseflow show that precipitation,
224 evaporites, silicates, and carbonates contribute $3.0 \pm 1.1\%$, $28.7 \pm 14.6\%$, $26.9 \pm 6.5\%$, and $41.4 \pm 13.2\%$,
225 respectively (Fig. 3a). During the typhoon event, the proportion of TDS at Nanxiong Bridge attributed
226 to TDS_{rain} is $6.3 \pm 2.4\%$. $TDS_{evaporite}$ contributes $32.4 \pm 13.6\%$ and increases from 27.4% to 61.1% at the
227 incipient first pulse. TDS_{sil} contributes $39.5 \pm 15.2\%$, which is 12.6% higher than the non-typhoon
228 period. TDS_{carb} contributes $21.8 \pm 11.5\%$ (Fig. 3b), which is 19.6% lower than the non-typhoon period.

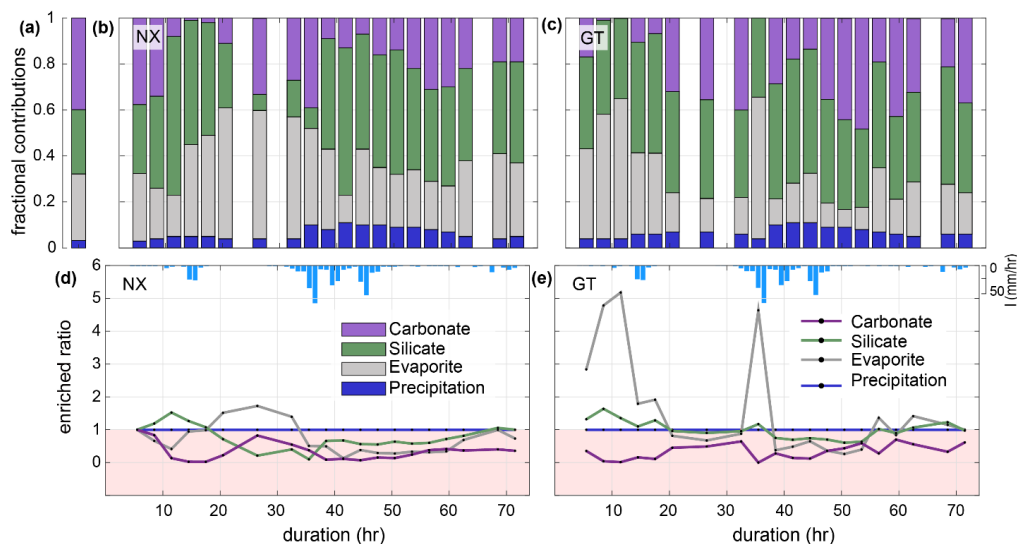
229 The fractional proportions of TDS at the Guting Bridge show that $6.5 \pm 2.1\%$ of TDS is contributed by
230 TDS_{rain} . $TDS_{evaporite}$ contributes $24.8 \pm 16.2\%$ and increases from 13.6% to 61.6% at the incipient second
231 pulse, when the SSC and SAR peak simultaneously. TDS_{sil} and TDS_{carb} contribute $39.5 \pm 15.2\%$ and
232 $27.5 \pm 16.7\%$, respectively (Fig. 3c).

233

234 Enriched ratios less than 1 indicate dilution, and values greater than 1 indicate concentration. Since we
235 set the ion concentration of rainfall to be constant during the typhoon event, the enriched ratio of
236 precipitation is constant throughout the observation period. At Nanxiong Bridge, the evaporites
237 enriched ratio increases from 0.4 to 1.7 between the two pulses and decreases to 0.1 at the discharge
238 peak. The silicates enriched ratio increases from 1 to 1.5 before the first pulse and decreases to 0.1 at
239 the peak of discharge, then returns to 1 before the observation ends. The concentration attributed to
240 carbonates is always diluted. The evaporites and carbonates enriched ratio have a statistically
241 significant negative correlation with discharge (evaporites: $\rho = -0.67$, carbonates: -0.60 , $p < 0.05$) and
242 the silicate enriched ratio has a negative correlation with discharge ($\rho = -0.32$), indicating dilution by
243 typhoon rainfall (Fig. 3d). At Guting Bridge, the evaporites enriched ratio has two peaks during the
244 two pulses with a value of 5.2 at the first peak, a value of 4.7 at the second peak. After the event, the
245 value returns to about 1.2. Notably, the evaporites enriched ratios during the both pulses are similar,



246 but the peak discharge of the second pulse is 5.5 times higher than that of the first pulse. The silicate
247 enriched ratio has an analogous pattern with the evaporites enriched ratio, but the enriched ratio is
248 smaller. Similar to Nanxiong Bridge, the carbonates enriched ratio is always diluted at Guting Bridge
249 (Fig. 3e). The evaporite and silicate enriched ratio shows a statistically significant positive correlation
250 ($\rho = 0.96, p < 0.05$), and the evaporite and silicate enriched ratios have a statistically significant positive
251 correlation with SAR ($\rho = 0.86, \rho = 0.84, p < 0.05$).



252
253 **Figure 3.** Timeseries illustrating TDS sources during the typhoon event at the two sampling sites.
254 Fig.3a shows the average proportion of TDS for the non-typhoon period from September 2014 to
255 December 2016 at Nanxiong Bridge; Fig.3b-c denotes the endmember contributions to TDS at
256 Nanxiong Bridge dataset and Guting Bridge dataset from the typhoon period; the purple bar denotes
257 TDS_{carb} (Eq. 8); green denotes TDS_{sil} (Eq. 7); the gray bar denotes $TDS_{evaporite}$ (Eq. 6); the blue bar
258 denotes TDS_{rain} (Eq. 4). Fig.3d-e denotes the enriched ratio of ion concentrations by TDS sources from
259 the Nanxiong Bridge dataset and Guting Bridge dataset during the typhoon period. The purple line
260 denotes TDS_{carb} , the green line denotes TDS_{sil} , the gray line denotes $TDS_{evaporite}$, the blue line denotes
261 the TDS_{rain} , and blue bar denotes hourly precipitation (I) at GTK station.

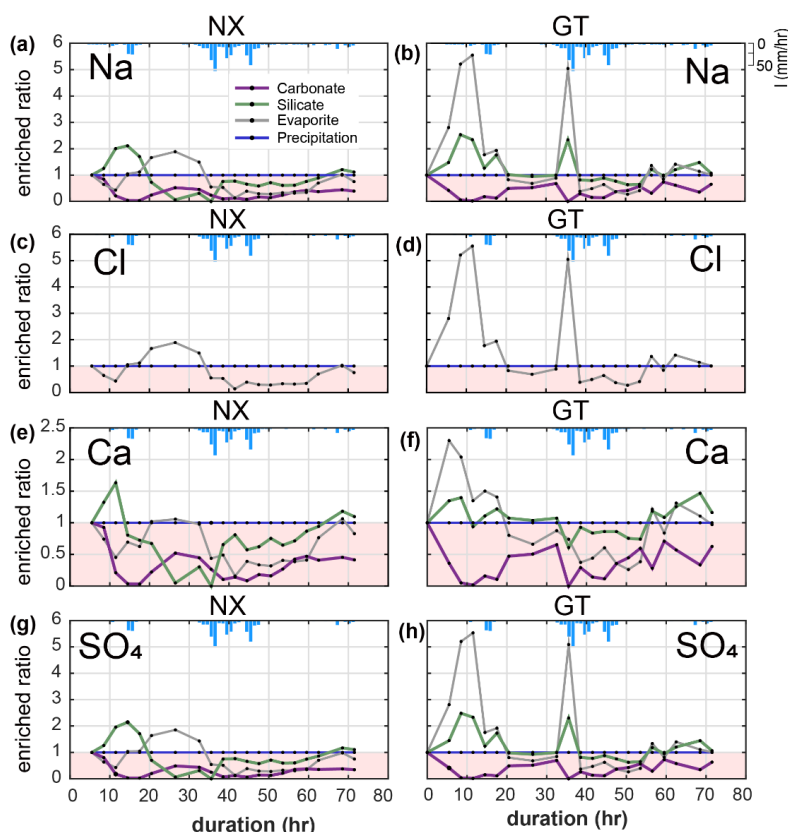


262 **4.2 Evaporite dissolution over time**

263 We calculated the enriched ratios of ions (i.e., Na^+ , Cl^- , Ca^{2+} and SO_4^{2-}) that are sourced from evaporites
264 (i.e., halite (NaCl) and gypsum (CaSO_4)). The variability in the concentrations of each of these ions
265 reflects the overall trends in TDS (Fig. 3d-e & Fig. 4).

266

267 At Nanxiong Bridge, all evaporite and carbonate ions have a statistically significant negative
268 correlation with discharge. The enriched ratios in evaporite Na^+ , Cl^- and SO_4^{2-} have the same trend (Fig.
269 4), which show an initial decrease during the first pulse, followed by an increase to 2 between the two
270 pulses, and a final decrease during the second pulse. Evaporite Ca^{2+} shows a similar trend with
271 evaporite Na^+ , Cl^- and SO_4^{2-} , but the values are below 1. The enriched ratios of silicate Na^+ , Ca^{2+} , and
272 SO_4^{2-} show an increase during the first pulse and a decrease to less than 1 before the rainfall peak,
273 followed by an increase from about 0.06 to 1.11 at the end of observation. At Guting Bridge, all
274 evaporite ions have a statistically significant positive correlation with the corresponding silicate ions
275 ($\text{Na}^+=0.98$; $\text{Ca}^+=0.81$; $\text{SO}_4^{2-}=0.98$, $p<0.05$). Evaporite Na^+ , Cl^- , and SO_4^{2-} each have two peaks that
276 occur prior to the maximum rainfall and reflect a factor of 5 increase in the enriched ratio. Compared
277 with Nanxiong Bridge (downstream), the enriched ratio in evaporite Ca^{2+} at Guting Bridge
278 concentrates at the onset of the first pulse and after peak discharge. Additionally, the enriched ratios of
279 carbonate at Guting Bridge are similar to Nanxiong Bridge, and are always below 1.



280

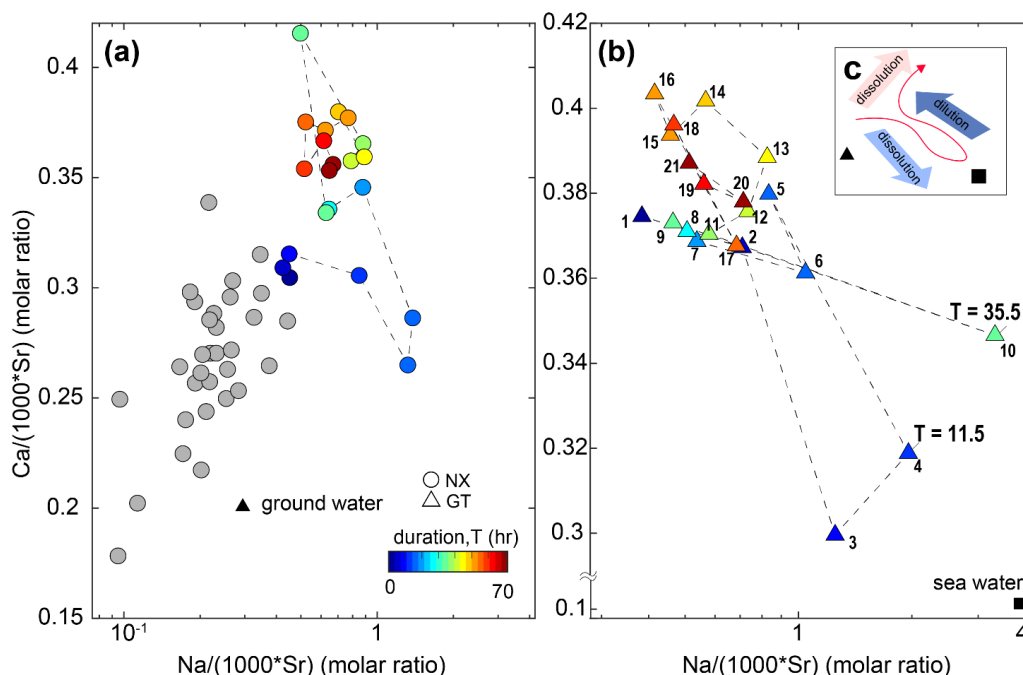
281 **Figure 4.** Time-series patterns in enriched ratio at two sampling sites. NX denotes the Naxiong Bridge
282 dataset and GT denotes Guting Bridge dataset. The pink area indicates enriched values below 1. Blue
283 bar denotes hourly precipitation (I) at Gutingkeng station.

284

285 Gaillardet et al. (1999) documented that dissolved ions ratios of Ca/Sr and Na/Sr are distinct for
286 carbonates (low Na/Sr, high Ca/Na) versus silicates or evaporites (high Na/Sr, low Ca/Na). We use
287 these ratios to elucidate potential mixing between carbonates and silicates/evaporites (Fig. 5). At
288 Naxiong Bridge, non-typhoon ratios of Na/(1000*Sr) and Ca/(1000*Sr) are 0.23–0.68 and 0.19–0.35,
289 respectively (Table S4). These values increase markedly during the typhoon events, with enriched
290 ratios of Na⁺ exceeding 5 at $T = 11.5$ and 35.5 hr. The high concentration of Na⁺, Cl⁻ and SO₄²⁻ (as
291 illustrated in the enriched ratio) indicate that there is enhanced dissolution of evaporites at the onset of
292 the typhoon event, especially at Guting Bridge. Subsequently, the concentration of Na⁺ decreased with



293 sustained rainfall. Then, the ratios approach the silicates/carbonates weathering (high Na/Sr, high
 294 Ca/Sr ratios) after the peak discharge.
 295



296
 297 **Figure 5.** Molar ratio mixing diagrams of Erren River waters for (a-b) Na/(1000*Sr) versus
 298 Ca/(1000*Sr), circles denote dataset at Nanxiong Bridge, and triangles denote dataset at Guting Bridge.
 299 Colorbar denotes survey duration. Gray circles denote the dataset at Nanxiong Bridge during baseflow
 300 conditions from 2014 to 2016. The black triangle illustrates the groundwater endmember (Chao et al.,
 301 2011); the black square illustrates the seawater endmember. Numbers in the triangle represent the time
 302 sequence, 1 represents the start point, and 21 represents the end point. (c) Illustration of dynamic
 303 weathering. The red line indicates the direction of change with time. The light blue arrow denotes
 304 dissolution of evaporite, the dark blue arrow denotes dilution from rainfall, and the red arrow denotes
 305 dissolution of suspended sediment.
 306

307 5. Discussion

308 5.1 Relationships between dissolved evaporite and river water chemistry

309 Before the survey, the monthly rainfall of the study area was 72.5 mm, which is only 18% of the
 310 average monthly rainfall, implying that it provides a relatively dry environment for accumulating



311 evaporites on the slope surface. Under maximum rainfall intensity, Na^+ , Cl^- and SO_4^{2+} at Guting Bridge
312 show markedly increased concentrations at the onset of the typhoon, peaks in enriched ratios that
313 exceed 5 (Fig. 4), and the greatest contribution of dissolved ions from evaporites (Fig. 3). In addition,
314 the sodium absorptions ratio (SAR) has a statistically significant positive correlation with $\text{TDS}_{\text{evaporite}}$
315 ($\rho = 0.86$, $p < 0.05$) at Guteng Bridge (upstream). During the typhoon event, the SAR increases from
316 4.8 to 24.9 and exceeds the threshold value of 13 at the incipient first pulse and at the incipient second
317 pulse. This pattern indicates that excess sodium is effective at inducing material dispersion and thus,
318 contributing to a higher suspended sediment load (Fig. 2).

319

320 These observations and results suggest that rainwater in the typhoon event rapidly dissolves the
321 evaporites on the slope surface, which produces high measured concentrations of Na^+ , Cl^- , and SO_4^{2+}
322 during the time of peak precipitation (30-40 hr of duration). Furthermore, the dissolution of the near-
323 surface evaporite deposits should be most heavily influenced by runoff from the hillslopes, so we
324 expect that excess sodium and enhanced erosion will be most significant on the hillslopes.

325

326 At Nanxiong Bridge, we observe a 10-hour delay in the peak enriched ratio relative to the SAR (Fig.
327 3d) and overall lower enriched ratios relative to Guteng Bridge (Fig. 3d-e). We suggest that dilution
328 and the transport distance from the badlands is responsible for this. The two catchments have a similar
329 areal extent of badlands within the total catchment area, which is about 2.49% at Nanxiong Bridge
330 catchment and 2.37 % in Guting Bridge catchment. Badlands contribute considerable evaporite solutes
331 (Chou, 2008), but the higher downstream drainage area will result in dilution of the solutes without
332 additional inputs. Additionally, Nakata and Chigira (2009) have observed that salt dissolution induces
333 an increase in electrical conductivity during intermittent rainfall events and decreases gradually after
334 rainfall events when evaporation and salt precipitate. Therefore, re-crystalization during transportation
335 is to be expected.



336

337 **5.2 From evaporite dissolution to silicate weathering**

338 Our observations show that the water chemistry of the typhoon event is dominated by silicate
339 weathering at 16.8 ton/km²/day, contributing 16.6% to the annual silicate weathering flux (Table S3).
340 Additionally, we observed a change in dominant chemical weathering mechanism during the typhoon
341 event. We rule out significant contributions from groundwater and deep seawater after peak discharge,
342 since ratios shift to higher Na/Sr, and Ca/Sr ratios relative to the non-typhoon ratio (Fig. 5a–b), and
343 the Ca/Sr ratio of mud volcanoes in the study site is one order of magnitude less than river water (Chao
344 et al., 2011). Carbonate weathering is the primary contributor of Ca²⁺ for most of the world's large
345 rivers (Gaillardet et al. 1999), but the increased Na⁺ and consistently enriched ratio of carbonate Ca²⁺
346 does not make this a likely contributor to the Erren River. We thus suggest that the primary contributor
347 to weathering is from enhanced silicate dissolution. This interpretation is supported by the temporal
348 evolution of the enriched ratio of silicate Ca²⁺, which gradually increases after the discharge peak, to
349 approach a value of about 1 at the end of survey (Fig. 4e&f). As such, in the waning of the event,
350 excess Ca²⁺ originates from a silicate source. Therefore, we suggest that the ratios shift to higher Na/Sr,
351 Ca/Sr ratios is due to silicate weathering. We also observe that the masses of Na and Ca are reduced
352 by 10.6% and 9.9%, respectively, in the suspended sediment during the course of the typhoon event
353 (Table S6).

354

355 Given that the sediment transported in the channel is supplied by physical erosion, we suggest that
356 physical erosion in our study site enhances silicate chemical weathering, which is consistent with
357 previous studies (Chung, 2002; Chou, 2008). Thus, we associate the change in weathering regime
358 during the course of the typhoon with abrasive erosion of silicate sediments in the channel. Mudstone
359 is mainly composed of silicate minerals (e.g., illite and chlorite minerals) (Tsai, 1984a), and few
360 swelling clay minerals (e.g., montmorillonite), which provide an abundant silicate pool. We suggest



361 that high suspended sediment concentrations combined with high energy flow during the typhoon,
362 caused increased silicate input from the weathered silicates in the suspended sediment. This trend can
363 explain about 10% of the reduced mass and it has also been observed on typhoon-driven silicate
364 chemical weathering from silicate minerals at surface (Meyer et. al., 2017). Importantly, the silicate
365 weathering flux that we calculate in this study is comparable to the global annual flux of rivers
366 (Gaillardet et al. 1999), suggesting that individual stochastic events may have global relevance.

367

368 **5.3 Typhoon-controlled cycles of physical and chemical erosion**

369 Evaporites, including halite (NaCl) and gypsum (CaSO₄), are found in few sedimentary environments,
370 and they are often excluded from global chemical weathering cycles (Gaillardet et al., 1999).
371 Compared to silicate rocks, the relation between evaporites weathering and physical erosion has rarely
372 been discussed. Through the interactions among riverine chemistry, suspended sediment properties,
373 and previous soil water chemistry studies, we suggest a positive feedback cycle of physical-chemical
374 erosion driven by mobile dissolved evaporite (Fig. 5). The feedback cycle includes three steps. (1)
375 precipitation and deposition of evaporite during the dry season in near-surface mudstone desiccation
376 cracks through capillary transport (Higuchi et al., 2013, 2015; Nakata and Chigira, 2009). In the dry
377 season, exposed bedrock with low water content develops desiccation cracks (Allen, 1982; Goehring
378 et al., 2010; Kindle, 1917; Seghir and Arscott, 2015; Xiaa and Hutchinson, 2000), providing space for
379 the re-precipitation of evaporite minerals. Using evidence from core samples in mudstone bedrock at
380 the study site, the depth of the crack of about 20 cm can be regarded as the thickness of the weathering
381 layer. Higuchi et al. (2013) suggested that the weathering layer in the top 10 cm of mudstone can easily
382 be eroded by intense rainfall. Erosion exposes fresh bedrock, which would dry in the following dry
383 season and further produce weatherable material.

384

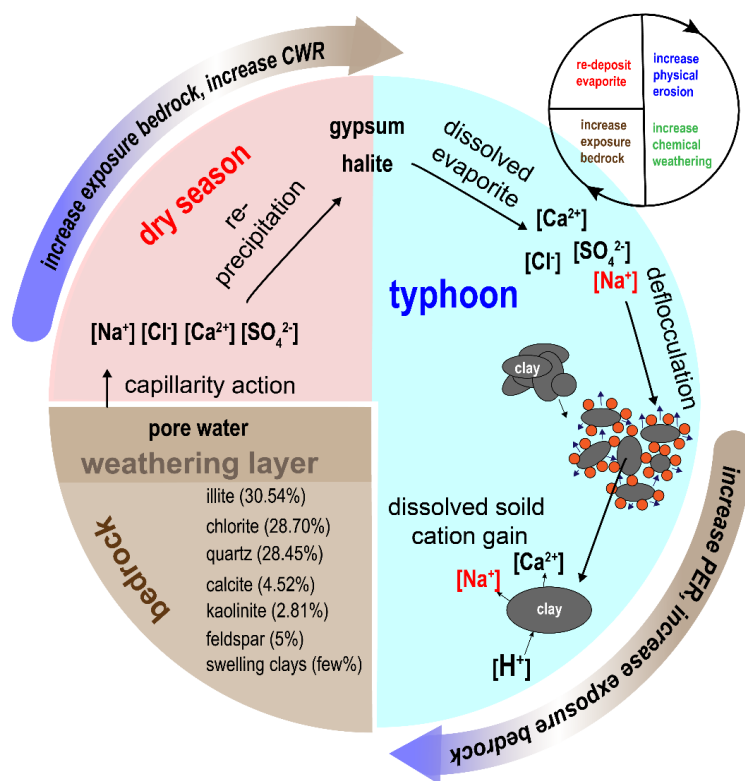
385 (2) Rainfall dissolves the evaporites, producing sodic water that increases physical erosion during
386 typhoon events. The resulting dissolved sodium causes higher hillslope erosion by deflocculation,



387 leading to increased suspended sediment in the channels. In the study site, hillslope erosion rate is
 388 about 9-30 cm/year (Higuchi et al., 2013; Yang et al., 2021a). At Nanxiong Bridge, the denudation rate
 389 approaches about 142,857 ton/km²/yr, measured from river suspended load (Dadson et. al., 2003), and
 390 the chemical weathering flux is 124-235 ton/km²/yr (Chou, 2008; this study). The high hillslope
 391 erosion rate ensures a steady supply of freshly exposed bedrock, allowing for high chemical weathering
 392 rates.

393

394 (3) Physical erosion enhances silicate weathering and bedrock exposure on hillslopes. Clay minerals
 395 in mudstone deposits are abraded from the abundantly available sediment and provide material for
 396 silicate weathering in streams. Ultimately, with frequent typhoon events and high temperatures in the
 397 study area, this dynamic cycle could repeat several times a year.



398

399 **Figure 6.** Cycle of feedback between physical erosion rate (PER) and chemical weathering rate (CWR)



400 in badlands catchment. Red blocks represent dry season conditions. Blue region represents typhoon
401 conditions. Brown region represents the bedrock and indicates the type and proportion of minerals of
402 mudstone (Tsai, 1984b).

403

404 **6. Conclusion**

405 We presented major element compositions of stream water from two sites in the Erren River catchment
406 at three-hour intervals during a three-day typhoon event in 2017. At the Guteng Station (upstream),
407 $TDS_{\text{evaporite}}$ is covariant with TDS_{sil} , the sodium adsorption ratio, and the suspended sediment
408 concentration, which can be assigned to dissolved evaporite (e.g., halite and gypsum). The excess
409 sodium in the evaporite deposits causes material dispersion through deflocculation, which enhances
410 the suspended sediment flux. Our observations show that the water chemistry of the typhoon event is
411 dominated by silicate weathering at $16.8 \text{ ton/km}^2/\text{day}$, in contrast with baseflow (non-typhoon)
412 conditions that are dominated by carbonate weathering. Moreover, during the course of the typhoon,
413 we observed a shift from predominantly evaporite weathering during peak precipitation to silicate
414 weathering at peak discharge.

415

416 Combining the observation of riverine chemistry, suspended sediment properties, and previous soil
417 water chemistry studies, we propose a feedback cycle between physical erosion and chemical
418 weathering in badlands topography, illustrating that precipitation of evaporites during the dry season
419 produces sodic water during typhoon events and preferentially triggers higher local erosion. The
420 enhanced hillslope erosion and abrasive effects of clay in a high discharge stream enhance bedrock
421 exposure on hillslopes and silicate weathering, respectively. Newly exposed bedrock then produces
422 more weathered material. Although measurements of bedrock mineral chemistry and Sr isotope are
423 still needed for confirming sources of excess sodium and calcium (Fig. 5), we suggest that the
424 conceptual model could provide an insight into landscape change of badlands. The results from our
425 study suggest that high erosion rates in mudstone badlands of the Erren River catchment is due to both
426 weakened lithology and to the interaction between evaporites and hillslope erosion.



427 *Data availability.* Relevant data supporting the findings of the study are available in the Supplementary
428 Information, or from the corresponding author upon request. Source data are provided with this paper.

429

430 *Author contributions.* C.-J.Y. designed the study and conducted field surveys, data analysis, and
431 modelling. P.-H. C. conducted data analysis. C.-J.Y., E. D. E. and J.M.T. wrote the paper with input
432 of all authors. S. X. conducted modelling. T. Y. T. provided the verified data. J.-C.L. and J.-C. Huang
433 contributed to the scientific discussion, interpretation, and paper preparation.

434

435 *Competing interests.* The authors declare that they have no competing interests.

436

437 *Acknowledgements.* This study was supported by grants from National Science and Technology
438 Council, Taiwan to Ci-Jian Yang (MOST 110-2917-I-564-009-).

439

440 **References**

- 441 1. Allen, J.R.L.: Sedimentary structures: Their Character and Physical Basis. Developments in
442 sedimentology. 30B, II. Elsevier, Amsterdam. 1982.
- 443 2. Burke, A., Present, T., Paris, G. Rae, Emily C.M., Sandilands, B. Gaillarde, J., Peucker-
444 Ehrenbrink, B., Fischer, W. W., McClelland, J. W., Spencer, R. G. M., Voss, B. M., Adkins, J. F.:
445 Sulfur isotopes in rivers: Insights into global weathering budgets, pyrite oxidation, and the
446 modern sulfur cycle. *Earth and Planetary Science Letters*, 496.
447 <https://doi.org/10.1016/j.epsl.2018.05.022ff.ffhal-02118784>, 2018
- 448 3. Calmels, D., Galy, A., Hovius, N., Bickle, M. J., West, A. J., Chen, M.-C., Chapman, H.:
449 Contribution of deep groundwater to the weathering budget in a rapidly eroding mountain belt,
450 Taiwan. *Earth and Planetary Science Letters*, 303 (1-2), 48–58.
451 <https://doi.org/10.1016/j.epsl.2010.12.032>, 2011
- 452 4. Carey, A. E., Gardner, C. B., Goldsmith, S. T., Lyons, W. B., Hicks, D. M.: Organic carbon yields



- 453 from small, mountainous rivers, New Zealand. *Geophysical Research Letters*, 32, 15404.
454 <https://doi.org/0.1029/2005GL023159>, 2005.
- 455 5. Chao, H.-C., You, C.-F., Wang, B.-S., Chung, C.-H., Huang, K.-F.: Boron isotopic composition of
456 mud volcano fluids: Implications for fluid migration in shallow subduction zones. *Earth and*
457 *Planetary Science Letters*, 305. <https://doi.org/10.1016/j.epsl.2011.02.033>, 2011.
- 458 6. Cheng, Y.-C., Yang, C.-J., Lin, J.-C.: Application for Terrestrial LiDAR on Mudstone Erosion
459 Caused by Typhoons. *Remote sensing*, 11(20), 2425. <https://doi.org/10.3390/rs11202425>, 2019.
- 460 7. Chou, C.-L.: Sediment Weathering and River Water Chemistry in the Erren Drainage Basin,
461 Southern Taiwan. Master thesis of Department of Earth Sciences, National Cheng Kung
462 University, 1–103, 2008.
- 463 8. Chung, S.-L.: Preliminary Geochemical and Isotopes study of the Erren river water. Master thesis
464 of Department of Earth Sciences, National Cheng Kung University, 1–95, 2002.
- 465 9. Clift, P. D., Wan, S., Blusztajn, J.: Reconstructing chemical weathering, physical erosion and
466 monsoon intensity since 25Ma in the northern South China Sea: A review of competing proxies.
467 *Earth-Science Reviews*, 130, 86–102. <https://doi.org/10.1016/j.earscirev.2014.01.002>, 2014.
- 468 10. Dadson, S. J., Hovius, N., Chen, H., Dade, W. B., Hsieh, M.-L., Willett, S. D., Hu, J.-C., Horng,
469 M.-J., Chen, M.-C., Stark, C. P., Lague, D. Lin, J.-C.: Links between erosion, runoff variability
470 and seismicity in the Taiwan orogen. *Nature*, 426(6967), 648–651,
471 <https://doi.org/10.1038/nature02150>, 2003.
- 472 11. Emberson, R., Hovius, N., Galy, A., Marc, O.: Chemical weathering in active mountain belts
473 controlled by stochastic bedrock landsliding. *Nature Geoscience*, 9, 42–47.
474 <https://doi.org/10.1038/ngeo2600>, 2016.
- 475 12. Faulkner, H., Alexander, R., Teeuw, R., Zukowskyj, P.: Variations in soil dispersivity across a
476 gully head displaying shallow sub-surface pipes, and the role of shallow pipes in rill initiation.
477 *Earth Surface Process and Landforms*. 29, 1143–1160. <https://doi.org/10.1002/esp.1109>, 2004.
- 478 13. Gaillardet, J., Dupre, B., Louvat, P., Allegre, C. J.: Global silicate weathering and CO₂



- 479 consumption rates deduced from the chemistry of large rivers. *Chemical Geology*, 159, 3–30.
480 [https://doi.org/10.1016/S0009-2541\(99\)00031-5](https://doi.org/10.1016/S0009-2541(99)00031-5), 1999.
- 481 14. Goehring, L., Conroy, R., Akhter, A., Cleggb, W.J., Routh, A.F.: Evolution of mud-crack patterns
482 during repeated drying cycles. *Soft Matter*, 6, 3562–3567. <https://doi.org/10.1039/B922206E>,
483 2010.
- 484 15. Hanson, B., Grattan, SR., Fulton, A.: *Agricultural salinity and drainage*. University of California
485 Irrigation Program, Davis., 1999.
- 486 16. Higuchi, K., Chigira, M., Lee, D.-H.: High rates of erosion and rapid weathering in a Plio-
487 Pleistocene mudstone badland, Taiwan. *Catena*, 106, 68–82.
488 <https://doi.org/10.1016/j.catena.2012.11.005>, 2013.
- 489 17. Higuchi, K., Chigira, M., Lee, D.-H., Wu, J.-H.: Rapid weathering and erosion of mudstone
490 induced by saltwater migration near a slope surface. *Journal of Hydrologic Engineering*, 20(6),
491 C6014004. [https://doi.org/10.1061/\(ASCE\)HE.1943-5584.0001105](https://doi.org/10.1061/(ASCE)HE.1943-5584.0001105), 2015.
- 492 18. Horneck, D.S., Ellsworth, J.W., Hopkins, B.G., Sullivan, D.M., Stevens, R.G.: *Managing Salt-
493 Affected Soils for Crop Production*. PNW 601-E. Oregon State University, University of Idaho,
494 Washington State University, 2007.
- 495 19. Kemeny, P. C., Torres, M. A.: Presentation and applications of mixing elements and dissolved
496 isotopes in rivers (MEANDIR), a customizable MATLAB model for Monte Carlo inversion of
497 dissolved river chemistry. *American Journal of Science*, 321(5), 579–642.
498 <https://doi.org/10.2475/05.2021.03>, 2021.
- 499 20. Kindle, E.M.: Some factors affecting the development of mud-cracks. *The Journal of Geology*,
500 25(2), 135–144. <https://doi.org/10.1086/622446>, 1917.
- 501 21. Lee, D.-H., Lin, H.-M., Wu, J.-H.: The basic properties of mudstone slopes in southwestern
502 Taiwan. *Journal of GeoEngineering*, 2(3), 81–95. [https://doi.org/10.6310/jog.2007.2\(3\).1](https://doi.org/10.6310/jog.2007.2(3).1), 2007.
- 503 22. Lee, Y.-J., Chen, P.-H., Lee, T.-Y., Shih, Y.-T., Huang, J.-C.: Temporal variation of chemical
504 weathering rate, source shifting and relationship with physical erosion in small mountainous
505 rivers, Taiwan, *Catena*, 190. <https://doi.org/10.1016/j.catena.2020.104516>, 2020.



- 506 23. Lu, S.-C. and Lin, N.-H.: Monitoring and component analysis of acid rain research
507 project. Environmental Protection Agency, Taiwan, 2014.
- 508 24. Lyons, W. B., Carey, A. E., Hicks, D. M., Nezat, C. A.: Chemical weathering in high-sediment-
509 yielding watersheds, New Zealand. *Journal of Geophysical Research-Earth Surface*, 110, 11.
510 <https://doi.org/10.1029/2003JF000088>, 2005.
- 511 25. Maher, K., and Chamberlain, C. P.: Hydrological Regulation of Chemical Weathering and the
512 Geologic Carbon Cycle. *Science*, 343, 1502–1504. <https://doi.org/10.1126/science.1250770>,
513 2014.
- 514 26. Meyer, K. J., Carey, A. E., You, C.-F.: Typhoon impacts on chemical weathering source
515 provenance of a High Standing Island watershed, Taiwan. *Geochimica et Cosmochimica Acta*,
516 215, 404–420. <https://doi.org/10.1016/j.gca.2017.07.015>, 2017.
- 517 27. Mitchell, J. K.: Volume change behavior. In: Mitchell, J.K., Soga, K. (Eds.), *Fundamentals of*
518 *Soil Behavior*. Wiley, 293–333, 1993.
- 519 28. Moon, S., Huh, Y., Qin, J.H., van Pho, N.: Chemical weathering in the Hong (Red) River basin:
520 Rates of silicate weathering and their controlling factors. *Geochimica et Cosmochimica Acta*, 71,
521 1411–1430. <https://doi.org/10.1016/j.gca.2006.12.004>, 2007.
- 522 29. Nadler, A., Levy, G. J., Keren, R., Eisenberg, H.: Sodic Calcareous Soil Reclamation as Affected
523 by Water Chemical Composition and Flow Rate. *Soil Science Society of America Journal*. 60 (1):
524 252. Bibcode:1996SSASJ.60.252N. <https://doi:10.2136/sssaj1996.03615995006000010038x>,
525 1996.
- 526 30. Nakata, E., Chigira, M.: Geochemistry of erosion processes on badland slopes. A case study of
527 the Gutingkeng formation where mud volcanoes are distributed in southern Taiwan. *Journal of*
528 *Geography*, 118(3), 511–532, 2009.
- 529 31. Negrel, P., Allegre, C.J., Dupre, B., Lewin, E.: Erosion sources determined by inversion of major
530 and trace element ratios and strontium isotopic ratios in river water: The Congo Basin case. *Earth*
531 *and Planetary Science Letters*, 120, 59–76. [https://doi.org/10.1016/0012-821X\(93\)90023-3](https://doi.org/10.1016/0012-821X(93)90023-3), 1993.



- 532 32. Rengasamy, P., Greene, R.S.B., Ford, G.W., Mehanni, A.H.: Identification of dispersive behavior
533 and the management of red-brown earths. *Australian Journal of Soil Research*, 22, 413–443.
534 <https://doi.org/10.1071/SR9840413>, 1984.
- 535 33. Rengasamy, P., Olsson, K. A.: Sodicity and soil structure. *Australian Journal of Soil Research*,
536 29, 935–952. <https://doi.org/10.1071/SR9910935>, 1991.
- 537 34. Seelig, B. D.: Salinity and Sodicity in North Dakota Soils. EB-57. North Dakota State University,
538 Fargo, ND, 2000.
- 539 35. Seghir, R., Arscott, S.: Controlled mud-crack patterning and self-organized cracking of
540 polydimeth. *Scientific Report*, 5, 14787. <https://doi.org/10.1038/srep14787>, 2015.
- 541 36. Sherard, J. L., Dunnigan, L. P., Decker, R. S., Steele, E. F.: Identification and nature of dispersive
542 soils. *Journal of the Geotechnical Engineering Division*, 102, 287–301. 1976.
- 543 37. Tsai, J. S.: The study on basic properties of mudstone and stabilization methods for mudstone
544 cut slope in southwestern Taiwan. Master Thesis of Civil Engineering Department, National
545 Cheng Kung University, Tainan, Taiwan, 1984b.
- 546 38. Xia, Z. C., Hutchinson, J. W.: Crack patterns in thin films. *Journal of the Mechanics and Physics*
547 *of Solids*, 48, 1107–1131. [https://doi.org/10.1016/S0022-5096\(99\)00081-2](https://doi.org/10.1016/S0022-5096(99)00081-2), 2000.
- 548 39. Yang, C.-J., Turowski, J. M., Hovius, N., Lin, J.-C., Chang, K.-J.: Badland landscape response to
549 individual geomorphic events. *Nature Communications*, 12(1):4631.
550 <https://doi.org/10.1038/s41467-021-24903-1>, 2021a.
- 551 40. Yang, C.-J., Jen, C.-H., Cheng, Y.-C., Lin, J.-C.: Quantification of mudcracks-driven erosion
552 using terrestrial laser scanning in laboratory runoff experiment. *Geomorphology*, 375.
553 <https://doi.org/10.1016/j.geomorph.2020.107527>, 2021b.
- 554 41. Yang, C.-J., Yeh, L.-W., Cheng, Y.-C., Jen, C.-H., Lin, J.-C.: Badland Erosion and Its
555 Morphometric Features in the Tropical Monsoon Area. *Remote sensing*, 11(24), 3051.
556 <https://doi.org/10.3390/rs11243051>, 2019.